

'100
'alf2' COMPUTATION OR
what is the
value for 'alf2'?
key value
ALF
you
alf2?
No! ALF you
'alf2'?
No
Yes → HERE'S
THE VALUE
IF 'alf2' was
just 100 then
we can just
jump to the
spot 100 in our
MANY.
1 YES
v.s.
99 NO's
1 YES.

Karla Stricker

Cummins, Inc.,
Box 3005,
Columbus, IN 47202

Lyle Kocher

Cummins, Inc.,
Box 3005,
Columbus, IN 47202

Ed Koeberlein

Cummins, Inc.,
Box 3005,
Columbus, IN 47202

D. G. Van Alstine

Caterpillar,
100 North East Adams Street,
Peoria, IL 61629

Gregory M. Shaver

School of Mechanical Engineering,
Purdue University,
585 Purdue Mall,
West Lafayette, IN 47907

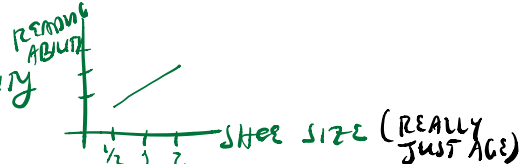
compresses
AIR
↓

Turbocharger Map Reduction for Control-Oriented Modeling

'AUTO-BOTS'
LOOKUP MAPS
ARE SLOW
INTERPOLATION
INACCURATE

Models of the gas exchange process in modern diesel engines typically use manufacturer-provided maps to describe mass flows through, and efficiencies of, the turbine and compressor based on pressure ratios across the turbine and compressor, as well as the turbocharger shaft speed, and in the case of variable-geometry turbochargers, the nozzle position. These look-up maps require multiple interpolations to produce the necessary information for turbocharger performance, and are undesirable when modeling for estimation and control. There have been several previous efforts to reduce dependence on maps with general success, yet many of these approaches remain complex and are not easily integrated into engine control systems. The focus of this paper is the reduction of turbomachinery maps to analytical functions that are amenable to estimator and control design, and have been validated against manufacturer-provided turbomachinery data. [DOI: 10.1115/1.4026532]

EX: LINEAR MODEL
SHOE SIZE v.s. READING ADJUST



geometry turbocharging (VGT). These equations, while physically motivated, are conditionally dependent on flow conditions inside the turbine or compressor, adding an extra layer of complexity to models intended for control design. One goal of this paper is to develop analytical models without any of these conditional dependencies.

More complex models have also been proposed. References [28] and [15] outline 2-zone models for the compressor; Ref. [15] describes a 7-zone model to describe turbine performance. Reference [3] outlines a turbine model based on 2D flow, while Ref. [29] proposes a detailed compressor model including slip factors, skin friction, and incidence losses. There have also been models derived directly from the Navier-Stokes equations [2,4,5], as well as investigations with artificial neural networks [30,31].

A non-dimensional approach, first proposed by Ref. [32], explored further by Ref. [33], is considered here. This approach reduces maps to analytical functions by transforming performance variables into non-dimensional parameters. This method has been utilized in a number of efforts [30,34–36], but has previously only been applied to describe compressor performance. New contributions outlined in this paper include:

- (1) The incorporation of turboshaft speed dependencies directly into the compressor non-dimensionalizations to simplify the resulting analytical expressions for compressor flow and efficiency.
- (2) The extension of the non-dimensionalization strategy to the turbine.

The development of simple, analytical descriptions of the compressor and turbine flows and efficiencies that maintain reasonable predictive capabilities and are concurrently control-amenable is the main focus of this work.

2 Compressor Map Reduction

Compressor mass flow and efficiency are transformed into non-dimensional parameters and fit with analytical functions as outlined in Secs. 2.1 and 2.2.

2.1 Compressor Mass Flow. As defined in Ref. [32], compressor work is expressed in terms of a non-dimensional head parameter Ψ_c ,

Contributed by the Dynamic Systems Division of ASME for publication in the JOURNAL OF DYNAMIC SYSTEMS, MEASUREMENT, AND CONTROL. Manuscript received March 30, 2011; final manuscript received May 18, 2012; published online April 4, 2014. Assoc. Editor: Marco P. Schoen.

PRESSURE RATIO (PR)
TURBOSHAFT SPEED (ω)
NOZZLE POSITION (X_{NS})

REMOVE AS MUCH AS POSSIBLE!

Models of the gas exchange process in modern diesel engines typically use manufacturer-provided maps to describe mass flows through, and efficiencies of, the turbine and compressor based on pressure ratios across the turbine and compressor, as well as the turbocharger shaft speed, and in the case of variable-geometry turbochargers, the nozzle position. These look-up maps require multiple interpolations to produce the necessary information for turbocharger performance, and are undesirable when modeling for estimation and control. There have been several previous efforts to reduce dependence on maps with general success, yet many of these approaches remain complex and are not easily integrated into engine control systems. The focus of this paper is the reduction of turbomachinery maps to analytical functions that are amenable to estimator and control design, and have been validated against manufacturer-provided turbomachinery data. [DOI: 10.1115/1.4026532]

SIMPLE SOLNS
ARE GOOD.

TURBINE	COMPRESSION	PR	w	MASS FLOW	EFFICIENCY

TWO ISSUES

- SLOW
- IMPRECISE
FOR KEYS NOT
IN THE MAP
PASSTHROUGH.

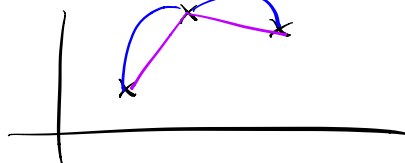
3 NUMBERS.

$$\begin{bmatrix} .17 & .68 & 3 \\ .19 & .68 & 3 \end{bmatrix} \text{ And the key is } [0.18 \quad 0.68 \quad 3]$$

WHAT'S THE REPORTED VALUE?

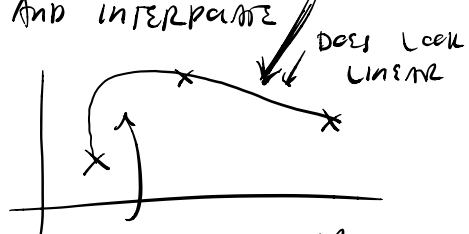
VALUE @ EACH MAP LOCATION (HERE WE ONLY NEED

2 POINTS; OFTEN WE MAY NEED MORE) AND INTERPOLATE
THEN.



WHY IS THIS OKAY?

LOCALLY LOTS OF THINGS ARE LINEAR



VERY NOT LINEAR
↳ A LOT OF ERROR.

CONTROL THEORY ISSUE: COMPUNDING ERROR! $\rightarrow [\theta_1 \quad \theta_2][x_1 \quad x_2]$

N.N. $\rightarrow f_\theta = \frac{dp}{dx}$ SAY f_θ IS LINEAR: $f_\theta(x) = \theta x = \theta_1 x_1 + \theta_2 x_2$

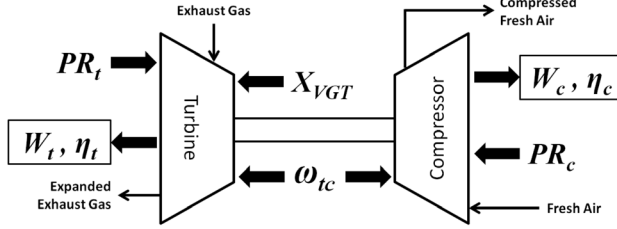
FIRST TIME

I WANT $p(T)$ TO BE OF VALUE P_f .

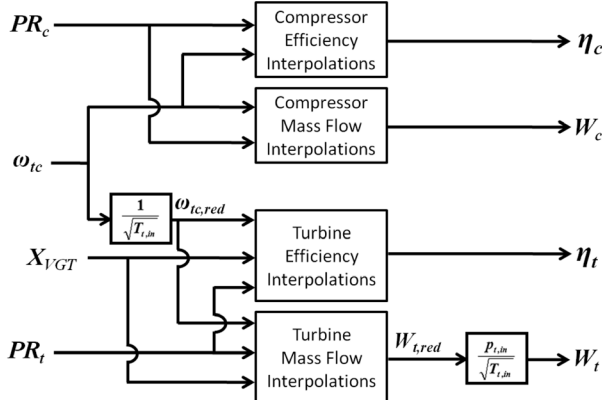
$$P_f = \int_0^T \frac{dp}{dx} dx = p(T) - p(0) = p(T).$$

LET $p(0)=0$

"NEUTR FLW"
EULER'S METHOD;
ACCUMULATING ERROR!



(a) Schematic of a variable-geometry turbocharger



(b) Input-to-output logic flow

Fig. 1 Variable-geometry turbocharger

$$\Psi_c \equiv \frac{\Delta h_c}{\frac{1}{2} U_c^2} \quad (1)$$

where U_c is the compressor blade tip speed given by

$$U_c \equiv \frac{\pi}{60} d_c \omega_{tc} \quad (2)$$

where ω_{tc} is the turbocharger shaft speed and d_c is the compressor blade tip diameter. In Eq. (1), Δh_c is the enthalpy change across the compressor,

$$\begin{aligned} \Delta h_c &\equiv c_p \Delta T = c_p (T_2 - T_1) \\ &= c_p T_1 \left(\frac{T_2}{T_1} - 1 \right) \end{aligned} \quad (3)$$

Assuming an isentropic compression process of an ideal gas, temperature and pressure are related by

$$\frac{T_2}{T_1} = \left(\frac{P_2}{P_1} \right)^{\frac{1}{\gamma}} \quad (4)$$

Substituting this into Eq. (3) gives

$$\begin{aligned} \Delta h_c &= c_p T_1 \left(\left(\frac{P_2}{P_1} \right)^{\frac{1}{\gamma}} - 1 \right) \\ &= c_{p,a} T_a \left(PR_c^{\frac{1}{\gamma}} - 1 \right) \end{aligned} \quad (5)$$

where PR_c is the pressure ratio across the compressor. T_a , $c_{p,a}$, and γ denote the temperature, specific heat and ratio of specific heats of the inlet air, taken at ambient conditions.

Combining Eqs. (1), (2), and (5) yields,

$$\Psi_c = \frac{c_{p,a} T_a \left(PR_c^{\frac{1}{\gamma}} - 1 \right)}{\frac{1}{2} \left(\frac{\pi}{60} d_c \omega_{tc} \right)^2} \quad (6)$$

The normalized compressor flow rate as defined in Ref. [32] is

$$\Phi_c \equiv \frac{W_c}{\frac{\pi}{4} \rho_a d_c^2 U_c} \quad (7)$$

where W_c is the mass flow rate through the compressor. ρ_a is the compressor inlet air density taken at ambient conditions.

To account for compressor speed variation, we introduce the compressor inlet Mach number,

$$M_c \equiv \frac{U_c}{\sqrt{\gamma R T_a}} \quad (8)$$

where R is the gas constant of ambient air. Using the inlet Mach number provides a mainly physically based method for incorporating rating speed while keeping the flow parameter non-dimensional.

Specifically, we propose a new dimensionless flow parameter, given by

$$\begin{aligned} \Phi'_c &\equiv \frac{\Phi_c^{\frac{\gamma-1}{\gamma}}}{M_c^{\frac{\gamma-1}{\gamma}}} = \frac{W_c}{\frac{\pi}{4} \rho_a d_c^2 U_c \left(M_c^{\frac{\gamma-1}{\gamma}} \right)} \\ &= \frac{W_c}{\frac{\pi}{4} \rho_a d_c^2 \left(\frac{1}{\gamma R T_a} \right)^{\frac{\gamma-1}{2\gamma}} \left(\frac{\pi}{60} d_c \omega_{tc} \right)^{\frac{2\gamma-1}{\gamma}}} \end{aligned} \quad (9)$$

Manufacturer-provided compressor mass flow map data is shown in Fig. 2(a). Traditionally, compressor maps are shown as pressure ratio versus mass flow; here the mass flow is plotted as a function of the pressure ratio across the compressor to emphasize the input-output relationship. Each line represents a different compressor speed (listed in krpm).

As seen in Fig. 2(a), for a given compressor speed (i.e., turbocharger shaft speed, ω_{tc}), as the pressure ratio across the compressor increases, mass flow decreases as it increasingly difficult to work against the rise in pressure. The flow drops off to a point that local flow reversal occurs. Eventually there is completely flow reversal, stalling the compressor and resulting in a drop in pressure. The dashed-dotted line in Fig. 2(a) is the stall line. Note that increases in compressor speed allow higher pressure ratios across the compressor before stall occurs.

On the other hand, as the pressure ratio decreases, mass flow increases. Eventually, with a low enough pressure ratio, the mass flow can reach sonic conditions within the compressor and become choked. At this point, substantially higher compressor speeds are necessary for an increase in mass flow, yet only a limited increase is possible. The dashed line in Fig. 2(a) marks the edge of the choke region.

Figure 2(b) shows the conversion of the map in Fig. 2(a) to a non-dimensional map using the parameters from Ref. [33], namely Ψ_c and Φ'_c (Eqs. (6) and (7)). As shown in Fig. 2(b), the mass flow lines collapse and fall relatively near each other, however a clear dependence on ω_{tc} , the compressor speed, can still be seen both in the shape and scale of each line. This is taken into account in Ref. [33] by separately fitting each mass flow line as a quadratic function of Ψ_c . Each quadratic coefficient is further described as a function of compressor inlet Mach number (Eq. (8)), which is effectively a function of compressor speed.

By converting the non-dimensional compressor map shown in Fig. 2(b) to a new non-dimensional map using Ψ_c (from Eq. (6)) and Φ'_c (from Eq. (9)), the speed lines collapse and fall much closer to each other, as shown in Fig. 2(c). A zoomed-in version of Fig. 2(c) is shown in Fig. 3, and it can be seen more clearly that in addition to the speed lines falling closer together (Fig. 2(c)), the relative distance between each line is also reduced. Because of the closeness of these speed lines, one single third-order polynomial can be fit to the non-dimensional mass flow curves,

$$\Phi'_c = a_1 \Psi_c^3 + a_2 \Psi_c^2 + a_3 \Psi_c + a_4 \quad (10)$$

The coefficients a_i were found using weighted least squares,

$$wAx = wB \Rightarrow x = (A^T WA)^{-1} A^T WB \quad (11)$$

where A and B are defined matrices, x is the array to be solved for, and w is a matrix containing the weights. Relating to Eq. (10), $A = [\Psi_c^3 \Psi_c^2 \Psi_c^1]$, $B = \Phi'_c$, and $x = [a_i]$. The weighting matrix w was constructed to emphasize the importance of the three lower speed lines, which is the region where the engine generally operates. Additionally, the coefficients a_i have no further dependence on compressor speed. Combining Eqs. (6), (9), and (10) and solving for compressor mass flow yields,

$$\begin{aligned} W_{c,est} = & \frac{\pi}{4} \rho_a d_c^2 \left(\frac{1}{\gamma R T_a} \right)^{\frac{\gamma-1}{2\gamma}} \left(\frac{\pi}{60} d_c \omega_{tc} \right)^{\frac{2\gamma-1}{\gamma}} \left(a_1 \left[\frac{c_{p,a} T_a \left(PR_c^{\frac{\gamma-1}{\gamma}} - 1 \right)}{\frac{1}{2} \left(\frac{\pi}{60} d_c \omega_{tc} \right)^2} \right] \right. \\ & + a_2 \left[\frac{c_{p,a} T_a \left(PR_c^{\frac{\gamma-1}{\gamma}} - 1 \right)}{\frac{1}{2} \left(\frac{\pi}{60} d_c \omega_{tc} \right)^2} \right]^2 \\ & \left. + a_3 \left[\frac{c_{p,a} T_a \left(PR_c^{\frac{\gamma-1}{\gamma}} - 1 \right)}{\frac{1}{2} \left(\frac{\pi}{60} d_c \omega_{tc} \right)^2} \right] + a_4 \right) \end{aligned} \quad (12)$$

As desired, the estimated mass flow rate through the compressor, $W_{c,est}$, is a function of only two inputs: the pressure ratio across the compressor, PR_c , and the turbocharger shaft speed, ω_{tc} . These are the same two inputs used to determine compressor mass flow conventionally via the compressor map look-up tables (per Fig. 12(b)).

Parameters specific to the compressor used in this study, as well as ambient conditions for Eq. (12), are listed in Table 1. Substituting these numbers into Eq. (12) yields

$$\begin{aligned} W_{c,est} = & \omega_{tc}^{1.2854} \left[5.5735 \times 10^{16} a_1 (PR_c^{0.2854} - 1)^3 \omega_{tc}^{-6} \right. \\ & + 2.5755 \times 10^9 a_2 (PR_c^{0.2854} - 1)^2 \omega_{tc}^{-4} \\ & \left. + 1.1902 \times 10^2 a_3 (PR_c^{0.2854} - 1) \omega_{tc}^{-2} + a_4 \right] \end{aligned} \quad (13)$$

Here it is easier to see that compressor mass flow depends only on pressure ratio and speed. For this particular compressor, values of a_i found via weighted least squares are listed in Table 2.

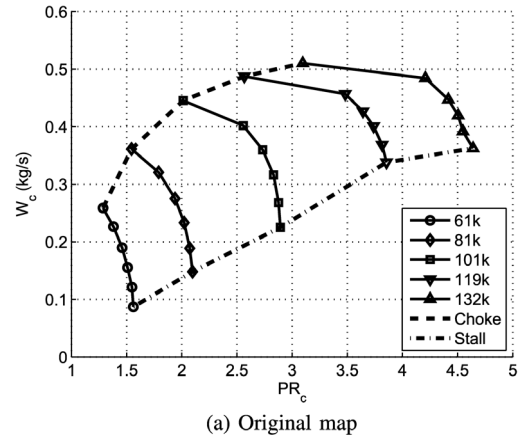
Using the estimated mass flow from Eq. (13), the compressor map was regenerated, as shown in Fig. 4. Some accuracy at the highest speed line is sacrificed in order to improve accuracy for the three lowest speed lines. Note that the manufacturer data, denoted by solid lines, is table-based, whereas the fitted data, denoted by dotted lines, are generated directly from Eq. (13).

2.2 Compressor Efficiency. Data from a manufacturer-provided compressor efficiency map is plotted in Fig. 5(a). For a given speed, efficiency increases with mass flow and peaks in the “heart” of the compressor map, then rapidly drops off toward the choke point. To collapse these efficiency lines in a fashion similar to compressor mass flow, the compressor efficiency was further “non-dimensionalized” by dividing the dimensionless head parameter by efficiency,

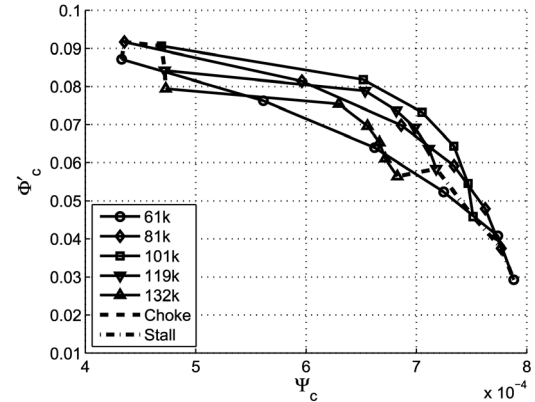
$$\eta'_c = \frac{\Psi_c}{\eta_c} \quad (14)$$

References [34] and [35] previously have presented Eq. (14) as a means to model compressor mass flow; here we use Eq. (14) for compressor efficiency instead.

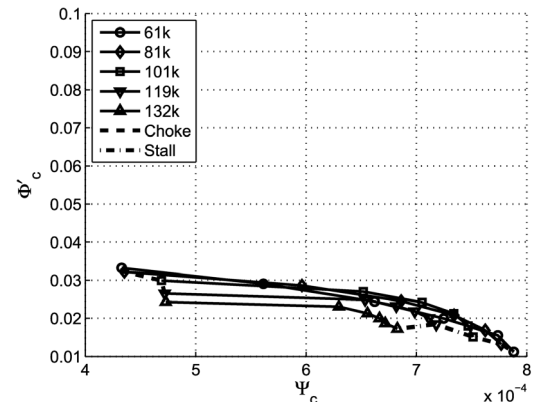
Figure 5(b) shows the transformation from the original compressor efficiency versus compressor flow data to non-dimensional



(a) Original map



(b) Non-dimensional map via (33)



(c) New non-dimensional map

Fig. 2 Compressor mass flow maps

compressor efficiency (η'_c), Eq. (14), versus non-dimensional compressor flow (Φ'_c), Eq. (9). Note that all of the speed lines collapse very close to each other and in a linear fashion.

The new efficiency variable η'_c was then fit to map data as a function of the dimensionless flow parameter,

$$\eta'_{c,est} = c_1 \Phi'_c + c_2 \quad (15)$$

Again, weighted least squares were used to determine the coefficients c_i , replacing the variables in Eq. (11) with the appropriate values from Eq. (15). Combining Eqs. (6), (7), (14), and (15) yields an expression for the estimated efficiency,

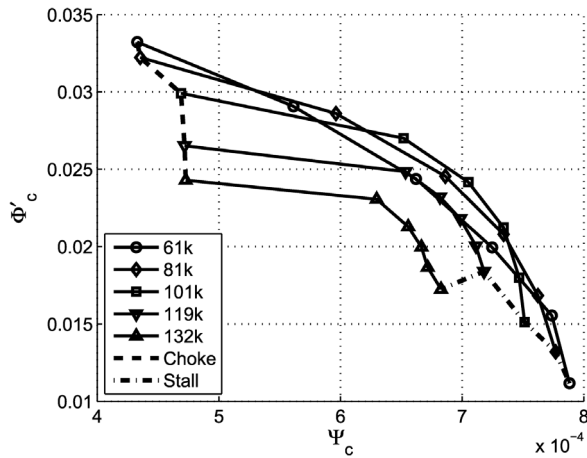


Fig. 3 New non-dimensional map: zoomed

Table 1 Compressor and ambient parameters

Parameter	Value	Units
T _a	300.5	K
ρ _a	1.149	kg/m ³
c _{p,a}	1.007	kJ/kg · K
Γ	1.3994	...
R	0.2871	kJ/kg · K
d _c	101	mm

Table 2 Compressor mass flow constants

a ₁	-1.0266 × 10 ⁹
a ₂	1.7206 × 10 ⁶
a ₃	-9.7634 × 10 ²
a ₄	0.2148

$$\eta_{c,est} = \frac{\left(c_{p,a} T_a \left(PR_c^{\frac{\gamma-1}{\gamma}} - 1 \right) \right)}{\left(\frac{1}{2} \left(\frac{\pi}{60} d_c \omega_{tc} \right)^2 \right)} \quad (16)$$

Substituting the parameters listed in Table 1 into Eq. (16) yields

$$\eta_{c,est} = \frac{2.164 \times 10^7 (PR_c^{0.2854} - 1)}{2.0549 \times 10^4 c_1 W_c \omega_{tc} + c_2 \omega_{tc}^2} \quad (17)$$

Here, W_c is the estimated compressor mass flow found using Eq. (13). The coefficients c_i found using weighted least squares are listed in Table 3. Thus, the only two inputs to estimated efficiency are the same as for estimated mass flow: the pressure ratio (PR_c) and turbocharger shaft speed (ω_{tc}). Using Eq. (17), estimated compressor efficiency can be compared to original compressor efficiency map data, shown in Fig. 6. As shown, the estimates match the map data very well, even at the highest two speed lines.

The non-dimensionalization method outlined in this section is similar to that described in Ref. [33], however the use of the newly defined non-dimensional mass flow parameter, Φ'_c (Eq. (9)), which directly incorporates the dependence on turbocharger speed, requires fewer overall coefficients needed to describe mass flow and efficiency here (6 coefficients from Eqs. (12) and (16)) than in previous efforts (15 coefficients in Refs. [30] and [33]).

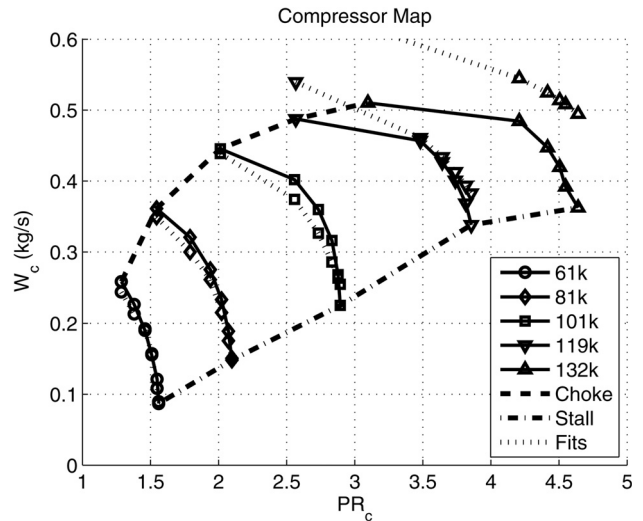


Fig. 4 Compressor map

3 Turbine Map Reduction

The majority of prior efforts make use of isentropic equations to model turbine flow and efficiency. When considering VGTs, an effective flow area is typically defined in terms of a VGT position and fit to experimental map data [2,20,24,25,30,33,34,37,38]. Many of these flow equations are conditionally dependent on whether the flow is choked or not, which adds another layer of complexity when considering control-oriented modeling. As stated, the non-dimensional approach outlined in Sec. 2 has previously been used to reduce compressor maps to analytical functions. We propose to apply this approach to the turbine, with some additional variations, and also reduce the VGT maps to analytical functions.

3.1 Turbine Mass Flow. The enthalpy change across the turbine is given by

$$\begin{aligned} \Delta h_t &\equiv c_p \Delta T = c_p (T_1 - T_2) = c_p T_1 \left(1 - \frac{T_2}{T_1} \right) \\ &= c_p T_1 \left(1 - \left(\frac{p_2}{p_1} \right)^{\frac{\gamma-1}{\gamma}} \right) \\ &= c_{p,exh} T_{t,in} \left(1 - \left(\frac{1}{PR_t} \right)^{\frac{\gamma-1}{\gamma}} \right) \\ &= c_{p,exh} T_{t,in} \left(1 - PR_t^{\frac{1-\gamma}{\gamma}} \right) \end{aligned} \quad (18)$$

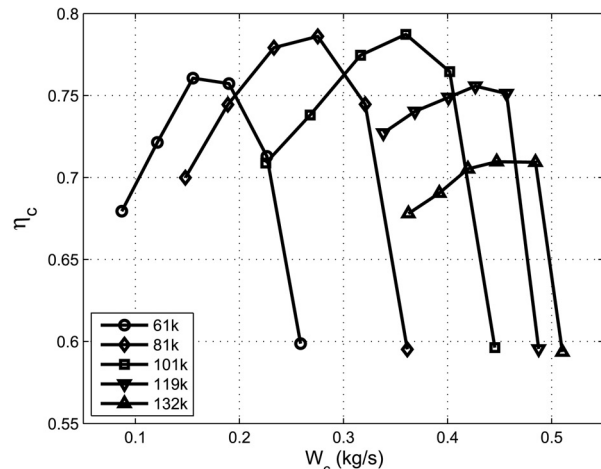
Here, $c_{p,exh}$ is the specific heat of the exhaust gas, PR_t is the pressure ratio across the turbine, and γ is the ratio of specific heats of the exhaust gas. Turbine maps generally express turbine speed and mass flow in terms of reduced quantities to account for inlet conditions,

$$W_{t,red} = \frac{W_t \sqrt{T_{t,in}}}{P_{t,in}} \quad (19)$$

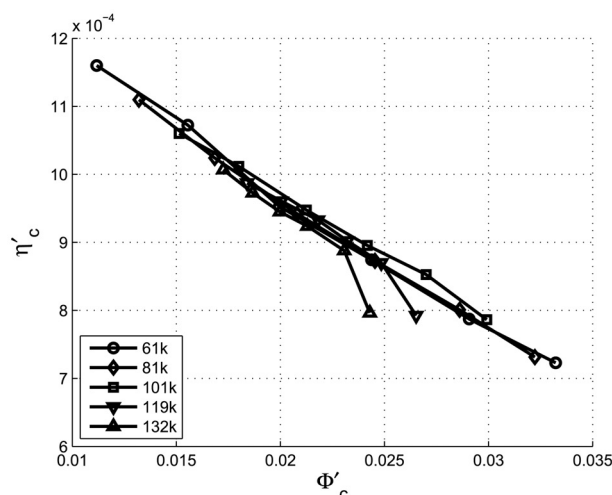
$$\omega_{tc,red} = \frac{\omega_{tc}}{\sqrt{T_{t,in}}} \quad (20)$$

where $T_{t,in}$ and $P_{t,in}$ are the turbine inlet temperature and pressure.

Implementing reduced mass flow ($W_{t,red}$) and turbocharger shaft speed ($\omega_{tc,red}$) into the non-dimensional parameters previously defined for the compressor (i.e., Eqs. (1) and (7)) yields slightly



(a) Original map



(b) Non-dimensional map

Fig. 5 Compressor efficiency maps

Table 3 Compressor efficiency constants

c_1	-1.9886×10^{-2}
c_2	1.3636×10^{-3}

different expressions for the turbine. The non-dimensional head parameter is now given by

$$\Psi_t \equiv \frac{\Delta h_t}{\frac{1}{2} U_t^2} = \frac{c_{p,\text{exh}} T_{t,\text{in}} \left(1 - PR_t^{\frac{1-\gamma}{\gamma}}\right)}{\frac{1}{2} \left(\frac{\pi}{60} d_t \omega_{tc}\right)^2} = \frac{c_{p,\text{exh}} \left(1 - PR_t^{\frac{1-\gamma}{\gamma}}\right)}{\frac{1}{2} \left(\frac{\pi}{60} d_t \omega_{tc,\text{red}}\right)^2} \quad (21)$$

and the dimensionless flow parameter is given by

$$\Phi_t \equiv \frac{W_t}{\frac{\pi}{4} \rho_{\text{exh}} d_t^2 U_t} = \frac{W_t}{\frac{\pi}{4} \rho_{\text{exh}} d_t^2 \left(\frac{\pi}{60} d_t \omega_{tc}\right)} = \frac{240 W_t R_{\text{exh}} T_{t,\text{in}}}{p_{t,\text{in}} \pi^2 d_t^3 \omega_{tc}} = \frac{240 W_{t,\text{red}} R_{\text{exh}}}{\pi^2 d_t^3 \omega_{tc,\text{red}}} \quad (22)$$

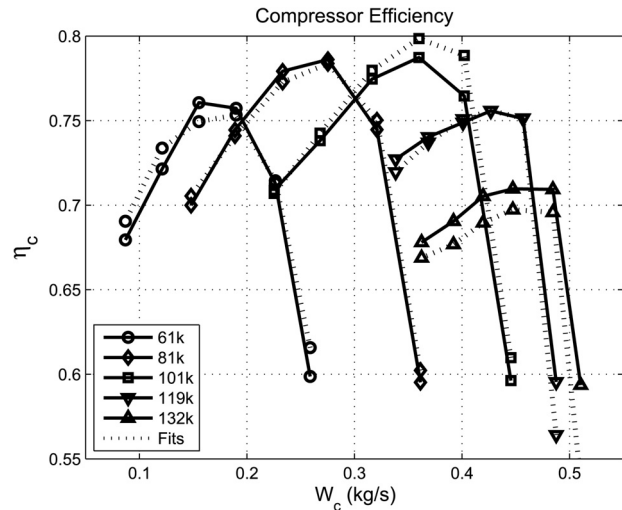


Fig. 6 Compressor efficiency

R_{exh} here is the gas constant of the exhaust gas. Further dependence on turbocharger shaft speed is introduced via the turbine inlet Mach number (M_t) and blade ratio (BSR),

$$M_t \equiv \frac{U_t}{\sqrt{\gamma R_{\text{exh}} T_{t,\text{in}}}} = \frac{\frac{\pi}{60} d_t \omega_{tc}}{\sqrt{\gamma R_{\text{exh}} T_{t,\text{in}}}} = \frac{\pi d_t \omega_{tc,\text{red}}}{60 \sqrt{\gamma R_{\text{exh}}}} \quad (23)$$

$$\begin{aligned} \text{BSR} &\equiv \frac{U_t}{\sqrt{2 c_{p,\text{exh}} T_{t,\text{in}} \left(1 - PR_t^{\frac{1-\gamma}{\gamma}}\right)}} \\ &= \frac{\frac{\pi}{60} d_t \omega_{tc}}{\sqrt{2 c_{p,\text{exh}} T_{t,\text{in}} \left(1 - PR_t^{\frac{1-\gamma}{\gamma}}\right)}} \\ &= \frac{\frac{\pi}{60} d_t \omega_{tc,\text{red}}}{\sqrt{2 c_{p,\text{exh}} \left(1 - PR_t^{\frac{1-\gamma}{\gamma}}\right)}} \end{aligned} \quad (24)$$

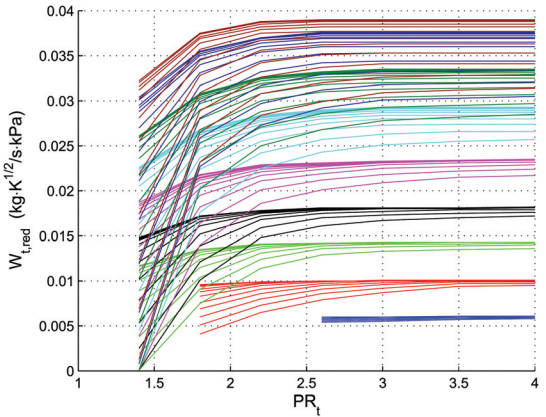
We include M_t and BSR in Eq. (22) and propose the following dimensionless flow parameter:

$$\Phi'_t = \Phi_t \cdot \frac{M_t^{\frac{1}{2}}}{\text{BSR}} = \frac{240 W_{t,\text{red}} R_{\text{exh}} M_t^{\frac{1}{2}}}{\pi^2 d_t^3 \omega_{tc,\text{red}} \text{BSR}} \quad (25)$$

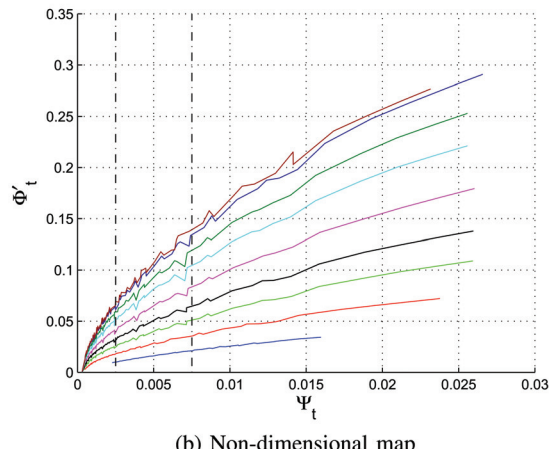
The transformation from the original turbine mass flow map to a non-dimensional map is shown in the top two plots of Fig. 7.

Manufacturer-provided map data for reduced mass flow plotted against turbine pressure ratio is shown in Fig. 7(a). Each of the nine sets of colored lines corresponds to a single VGT nozzle position, listed in Table 4 as a normalized rack position, X_{VGT} . Within a single VGT position, the different lines correspond to different turbocharger shaft speeds (12 speeds per VGT position). $\omega_{tc,\text{red}}$ decreases as shaft speed increases for a given X_{VGT} setting. For a given turbocharger shaft speed, mass flow through the turbine increases as the pressure ratio, PR_t (i.e., pressure drop), across the turbine increases. As the VGT closes, mass flow decreases, since a smaller VGT position results in a smaller effective blade area for the exhaust gas to impinge, decreasing the ability of the exhaust to drive the turbine.

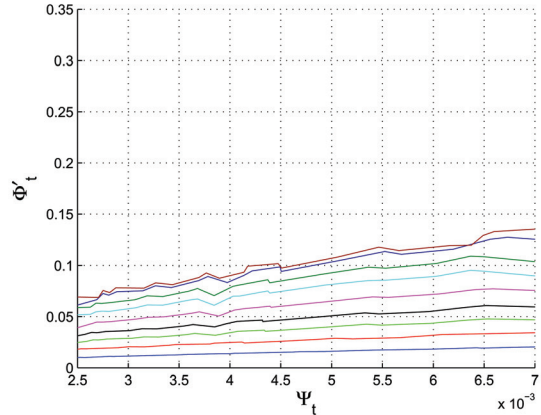
The original map in Fig. 7(a) was transformed to the non-dimensional parameters Ψ_t and Φ'_t , and Fig. 7(b) shows the non-dimensional flow (Φ'_t) plotted against the dimensionless head parameter (Ψ_t). The benefit of the non-dimensionalization is significant—a reduction from 108 lines in Fig. 7(a) to only 9 lines



(a) Original map



(b) Non-dimensional map



(c) Magnified range of interest

Fig. 7 Original and non-dimensional turbine mass flow maps

in Fig. 7(b), one for each of the nine VGT positions. As such, speed dependence is now incorporated in each of the nine lines via inclusion of the inlet Mach number and BSR into Φ'_t (Eq. (25)).

During engine operation, only a particular range of Ψ_t is experienced, denoted by the vertical dashed lines in Fig. 7(b). Figure 7(c) zooms in on this range of interest. These curves were then approximated as a linear function of the square root of Ψ_t ,

$$\Phi'_{t,est} = s_m (b_1 + b_2 \sqrt{\Psi_t}) \quad (26)$$

Coefficients b_1 and b_2 were fixed to fit the largest turbine map, corresponding to the most open VGT position ($X_{VGT}=1$), indicated by the top line in Fig. 7(c). Weighted least squares were employed here again to emphasize the important range of Ψ_t . The

Table 4 VGT position key

Color	X_{VGT}
Blue	0.0739
Red	0.1313
Green	0.2014
Black	0.2614
Magenta	0.3523
Cyan	0.4539
Dark Green	0.5499
Dark Blue	0.7658
Dark Red	1

scaling parameter, s_m , in Eq. (26) was then introduced as a quadratic function of VGT position to fit the smaller maps,

$$s_m = \alpha_1 X_{VGT}^2 + \alpha_2 X_{VGT} + \alpha_3 \quad (27)$$

Least squares were used to fix the values of α_i in Eq. (27). With this scaling parameter, Eq. (26) becomes

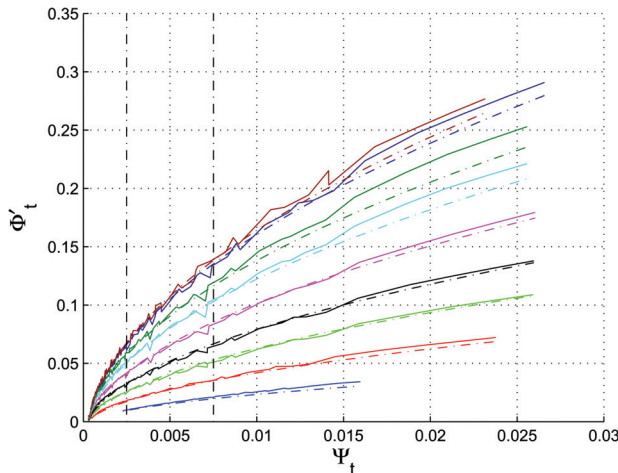
$$\Phi'_{t,est} = (\alpha_1 X_{VGT}^2 + \alpha_2 X_{VGT} + \alpha_3) (b_1 + b_2 \sqrt{\Psi_t}) \quad (28)$$

Plots of the fit from Eq. (28) against non-dimensional map data are shown in Fig. 8, again with the bottom plot showing the range of interest for Ψ_t .

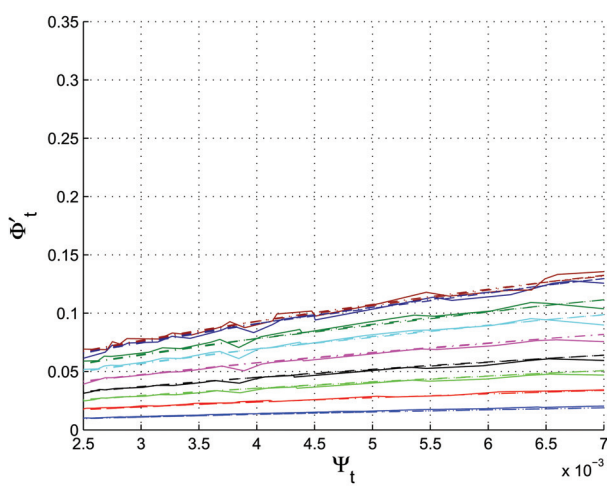
By combining Eqs. (21), (23)–(25), and (28), we can solve for reduced turbine mass flow, $W_{t,red}$, in terms of turbine pressure ratio (PR_t) and reduced turbocharger shaft speed ($\omega_{tc,red}$),

$$\begin{aligned} \Phi'_{t,est} &= (\alpha_1 X_{VGT}^2 + \alpha_2 X_{VGT} + \alpha_3) (b_1 + b_2 \sqrt{\Psi_t}) \\ &= (\alpha_1 X_{VGT}^2 + \alpha_2 X_{VGT} + \alpha_3) \left(b_1 + b_2 \sqrt{\frac{c_{p,exh} \left(1 - PR_t^{\frac{1-\gamma}{\gamma}}\right)}{\frac{1}{2} \left(\frac{\pi}{60} d_t \omega_{tc,red}\right)^2}} \right) \\ &= \frac{240 W_{t,red} R_{exh} M_t^{\frac{1}{\gamma}}}{\pi^2 d_t^3 \omega_{tc,red} BSR} \\ &= \frac{240 W_{t,red} R_{exh}}{\pi^2 d_t^3 \omega_{tc,red}} \left(\frac{\pi}{60} d_t \omega_{tc,red} \right)^{\frac{1}{\gamma}} \left(\frac{\sqrt{2 c_{p,exh} \left(1 - PR_t^{\frac{1-\gamma}{\gamma}}\right)}}{\frac{\pi}{60} d_t \omega_{tc,red}} \right) \\ &\Downarrow \\ W_{t,red} &= \pi d_t^2 (\gamma R_{exh})^{\frac{1}{2\gamma}} \left[b_1 + b_2 \sqrt{\frac{2 c_{p,exh} \left(1 - PR_t^{\frac{1-\gamma}{\gamma}}\right)}{\left(\frac{\pi}{60} d_t \omega_{tc,red}\right)^2}} \right] \\ &\times \frac{(\alpha_1 X_{VGT}^2 + \alpha_2 X_{VGT} + \alpha_3) \left(\frac{\pi}{60} d_t \omega_{tc,red}\right)^{\frac{2\gamma-1}{\gamma}}}{4 R_{exh} \sqrt{2 c_{p,exh} \left(1 - PR_t^{\frac{1-\gamma}{\gamma}}\right)}} \end{aligned} \quad (29)$$

Here, R_{exh} and $c_{p,exh}$ are assumed to be constant. The values for b_i and α_i , found via least squares, are listed in Table 5. Note that the three inputs to Eq. (29) are the same three inputs used to interpolate mass flow from the conventional turbine look-up maps, namely $\omega_{tc,red}$, PR_t , and X_{VGT} (per Fig. 1(b)), and result in reduced mass flow—the same output given by look-up maps. This reduced



(a) Non-dimensional map



(b) Magnified range of interest

Fig. 8 Non-dimensional turbine maps with fits

mass flow can then be used in Eq. (19) to back out actual mass flow through the turbine, similar to what is done to determine actual mass flow from turbine maps.

3.2 Turbine Efficiency. As was done with compressor efficiency, the turbine efficiency can also be “non-dimensionalized.” In this case, the non-dimensionalization is as follows:

$$\eta'_t = \frac{\eta_t \cdot \Psi_t^{\frac{\gamma-1}{\gamma}}}{M_t^\gamma} \quad (30)$$

Figure 9(a) shows the manufacturer-provided turbine map data for efficiency plotted against BSR, and Fig. 9(b) is the non-dimensional map data plotted against BSR. Note that, like turbine mass flow, this choice in non-dimensionalizing turbine efficiency reduces a turbine efficiency map containing 108 lines (Fig. 5(a)) down to one containing just 9 (Fig. 5(b)). Dashed black lines on this plot indicate the range of BSR seen during engine operation, and Fig. 9(c) magnifies this range of interest. The different colors signify different VGT positions (per Table 4).

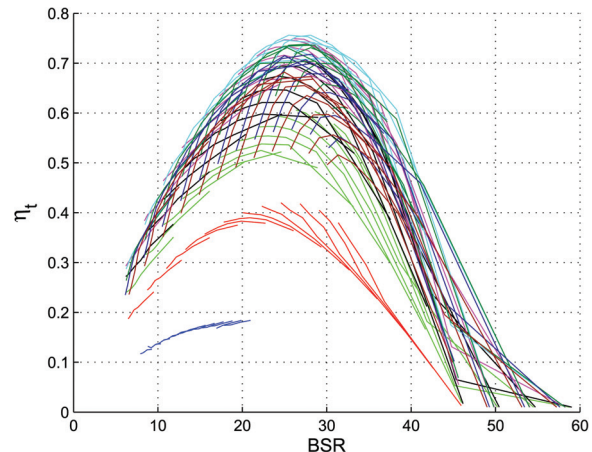
η'_t can be fit as an inverse function of BSR,

$$\eta'_{t,est} = s_e \left(k_1 + \frac{k_2}{BSR} \right) \quad (31)$$

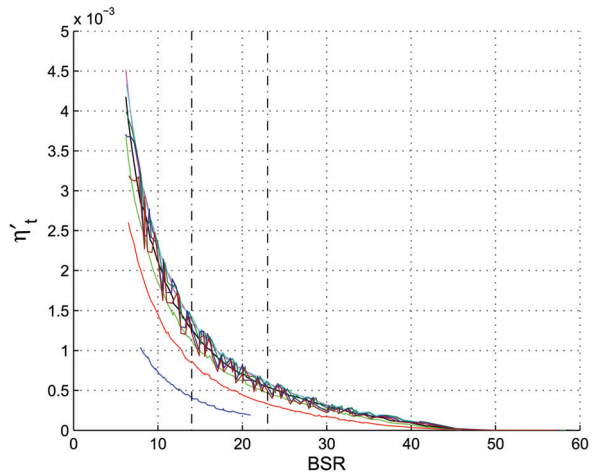
Similar to turbine mass flow, coefficients k_1 and k_2 in Eq. (31) are fixed to fit to the largest turbine map, corresponding to the most

Table 5 Turbine mass flow constants

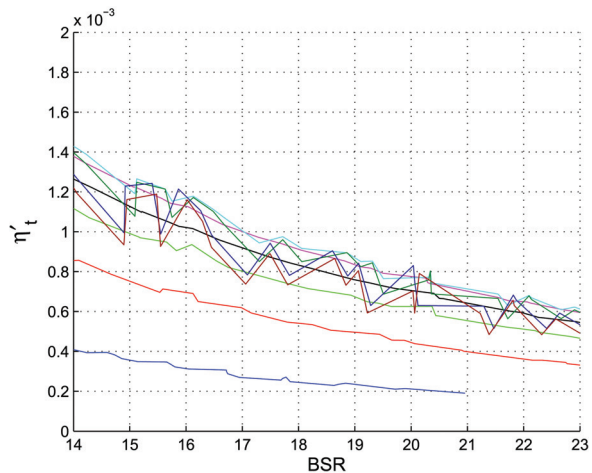
B_1	B_2	α_1	α_2	α_3
-2.8883×10^{-2}	1.9318	-1.2056	2.2198	-1.5203×10^{-2}



(a) Original map



(b) Non-dimensional map



(c) Magnified range of interest

Fig. 9 Original and non-dimensional turbine efficiency maps

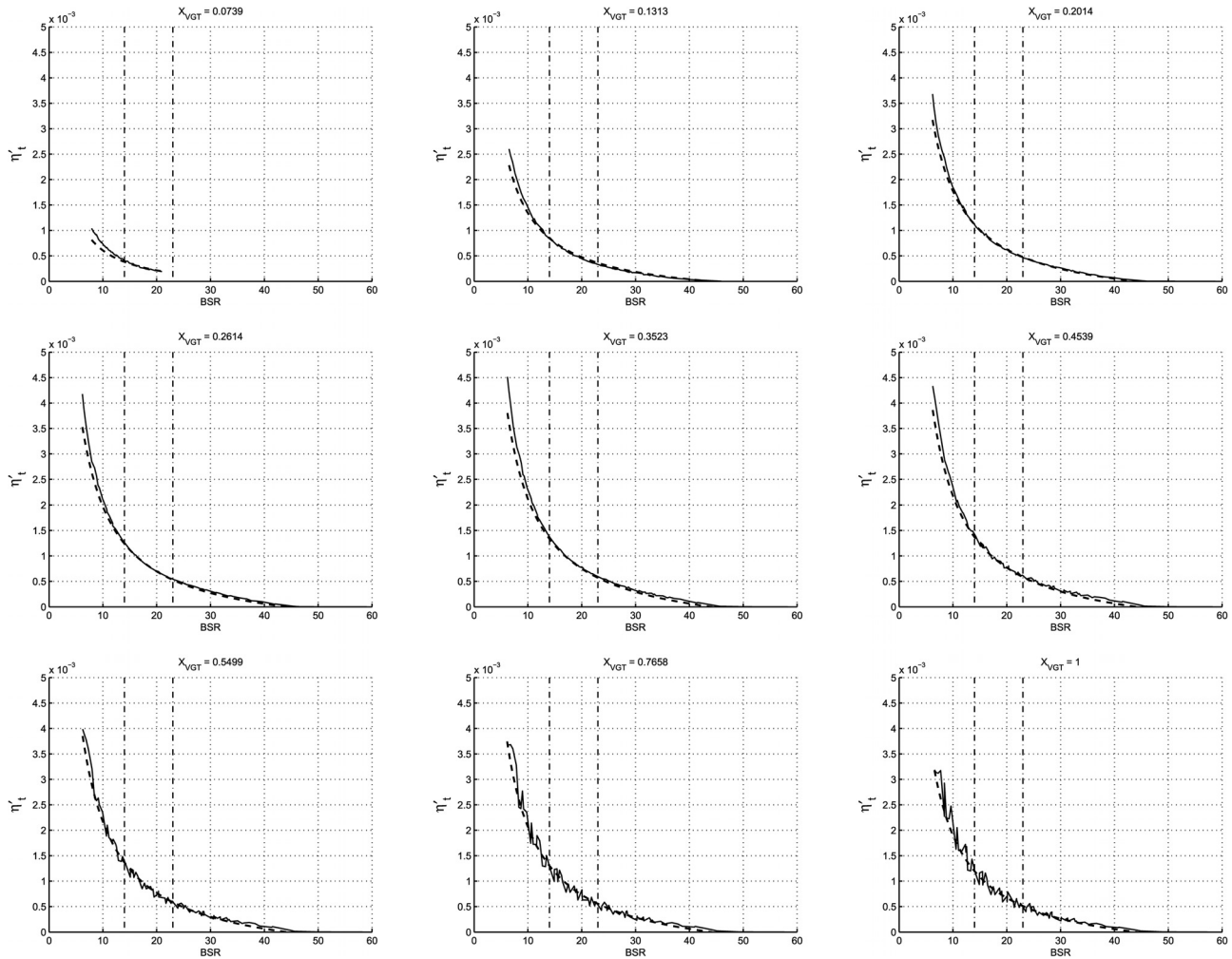


Fig. 10 Non-dimensional efficiency fits for the nine VGT positions

open VGT position ($X_{VGT} = 1$). A scaling parameter, s_e , is introduced to fit the smaller maps, and is a function of VGT position,

$$s_e = \beta_1 - \beta_2 \exp(-\beta_3 X_{VGT}) - \beta_4 \ln(X_{VGT}) \quad (32)$$

Note that for seven of the VGT settings in Fig. 9(b), one fit of η'_t versus BSR would be appropriate, such that s_e in Eq. (32) is constant.

Figure 10 shows the fits from Eqs. (31) and (32) against non-dimensional map data for each of the nine VGT positions. Though the efficiency fit (Eq. (31)) was weighted to a particular range of BSR, the fits match non-dimensional map data well even outside of this range.

By combining Eqs. (21), (30), (31), and (32), we can rearrange and solve for estimated turbine efficiency in terms of turbine pressure ratio (PR_t) and reduced turbocharger shaft speed ($\omega_{tc,red}$),

$$\begin{aligned} \eta_{t,est} &= [\beta_1 - \beta_2 \exp(-\beta_3 X_{VGT}) - \beta_4 \ln(X_{VGT})] \\ &\times \left(k_1 + k_2 \sqrt{\frac{2c_{p,exh} \left(1 - PR_t^{\frac{1-\gamma}{\gamma}}\right)}{\left(\frac{\pi}{60} d_t \omega_{tc,red}\right)^2}} \right) \\ &\times \frac{\left(\gamma R\right)^{\frac{1-\gamma}{2\gamma}} \left(\frac{\pi}{60} d_t \omega_{tc,red}\right)^{\frac{3\gamma-1}{\gamma}}}{2c_{p,exh} \left(1 - PR_t^{\frac{1-\gamma}{\gamma}}\right)} \end{aligned} \quad (33)$$

Table 6 Turbine efficiency constants

k_1	k_2	β_1	β_2	β_3	β_4
-5.6245×10^{-4}	2.4509×10^{-2}	-0.8619	-3.7730	0.7127	-0.9268

Again, $c_{p,exh}$ and R_{exh} are assumed to be constant here. Values for coefficients k_i and β_i are listed in Table 6. Again, note that the three inputs to Eq. (33) are the same three inputs used to interpolate turbine efficiency from the traditional turbine look-up maps, namely ω_{tc} , PR_t , and X_{VGT} (per Fig. 1(b)). Equation (33) can therefore be used to analytically determine the turbine efficiency. Figure 11 shows estimated turbine efficiency calculated via Eq. (33) compared to the original turbine efficiency map data.

For small X_{VGT} , the estimated turbine efficiency (per Eq. (33)) corresponds well with map data; however, for the three largest VGT positions, the fits are not as accurate. The non-dimensional map data for these three largest VGT positions, per Fig. 10, show some variability in the non-dimensional efficiency as a function of BSR. The analytical functions are a best-fit model of this map data, and as such the discrepancies between the model (dashed lines) and the map data (solid lines) are magnified when the scaling parameter, s_e , is implemented per Eqs. (31)–(33).

4 Comparison to Turbocharger Maps

Figure 1(b) is displayed again in Fig. 12 comparing the flow of inputs to outputs for determining turbine and compressor flows and efficiencies using manufacturer-provided maps (Fig. 12(a))

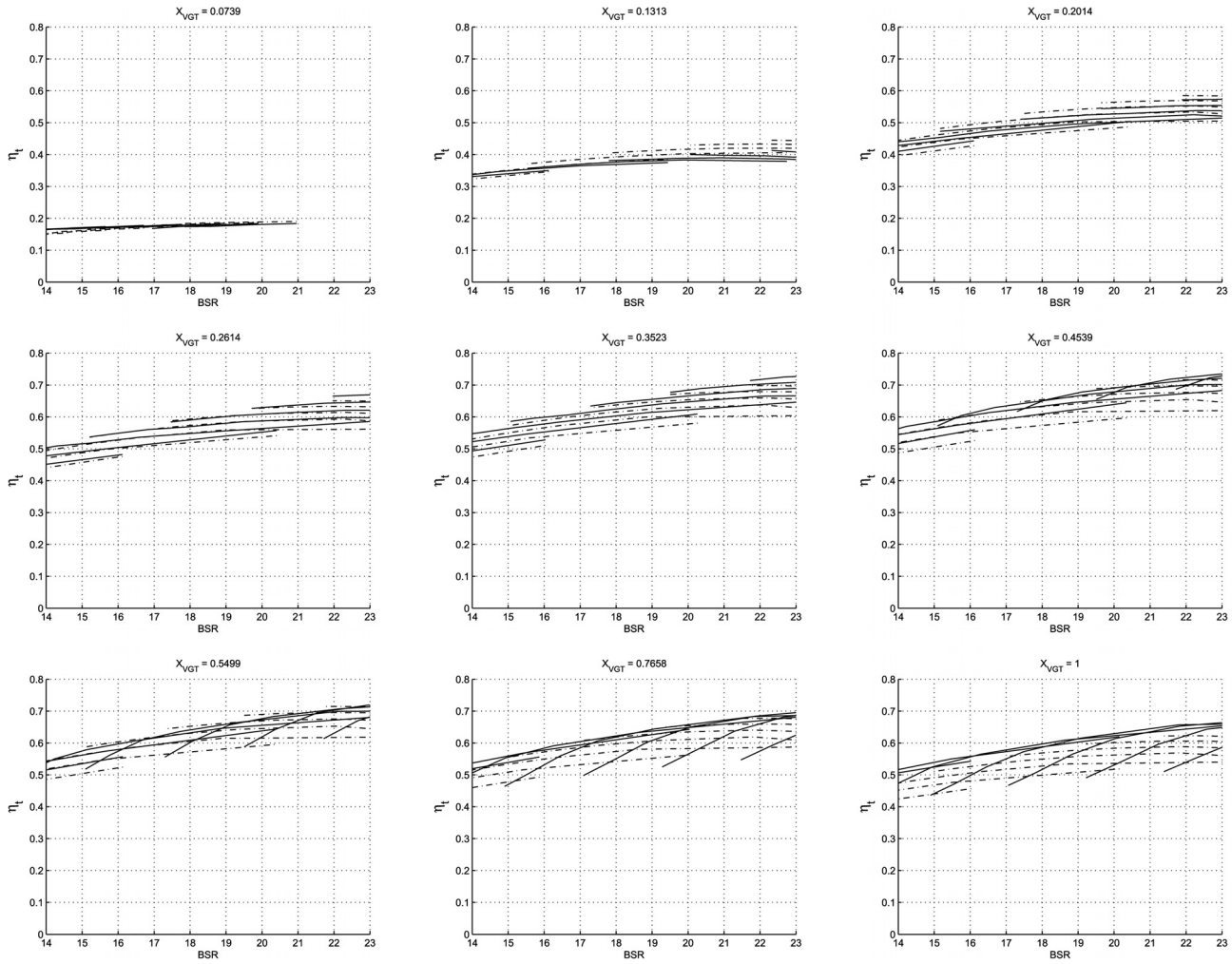


Fig. 11 Efficiency fits for the nine VGT positions

and the analytical functions previously described in Secs. 2 and 3 (Fig. 12(b)).

While the mapping from inputs to outputs using turbocharger maps may seem simpler at first glance, remember that by using turbocharger maps, mass flow and efficiency is determined as a result of multiple interpolations from large look-up tables. On the other hand, mapping from inputs to outputs using the method displayed in Fig. 12(b) is purely analytical and requires no conditional logic or interpolations. Because of this, the non-dimensionalization method outlined in Secs. 2 and 3 (Eqs. (12), (16), (29), and (33)) is beneficial for model-based estimator and control design.

5 Turbocharger Model Application

The functions detailed above for the mass flows and efficiencies of the compressor and turbine (see Fig. 12(b)) are ultimately intended for use in control-oriented models. One use case is replacing the manufacturer-provided turbocharger maps with the approach in Fig. 12(b) in a reduced-order MATLAB engine simulation model [39], used primarily to simulate the gas exchange processes of a multi-cylinder diesel engine, a schematic of which is shown in Fig. 13.

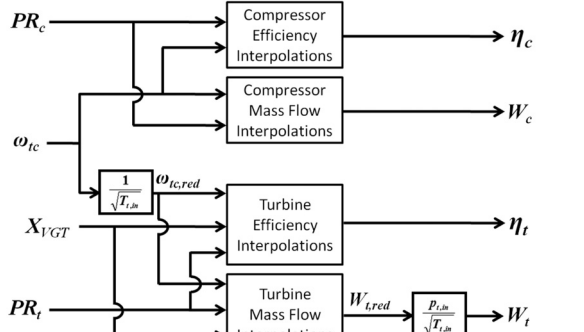
The gas exchange model was run to simulate steady-state engine performance during “air-handling sweeps.” During these tests, at three fixed exhaust gas recirculation (EGR) valve positions, the VGT nozzle is swept from open to closed, and steady-state engine data is taken at each VGT nozzle position (X_{VGT} in

Fig. 13). Likewise, for three fixed VGT positions, the EGR valve is swept from closed to open. The coordinated use of these two actuators determines the amount of charge (a mixture of fresh air and recirculated exhaust gas, or EGR) and EGR fraction (the fraction of exhaust gas in the charge gases) that flow into the intake manifold. Engine air-handling system behavior is then characterized by plotting EGR fraction against charge flow, shown in an example air-handling sweep plot in Fig. 14.

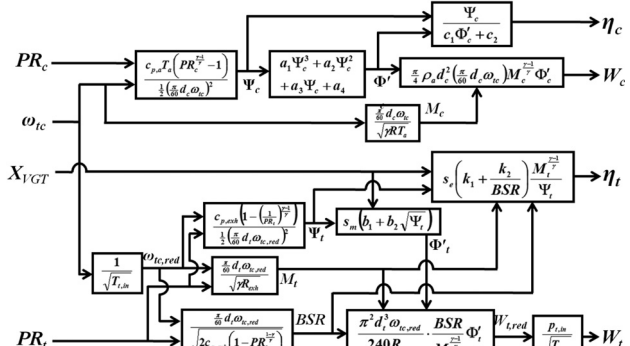
Looking at Fig. 14, it can be seen that for a fixed EGR position, charge flow increases as the VGT is closed. After a certain point, however, charge flow ceases to increase and instead decreases even as the VGT keeps closing. This is because turbine efficiency peaks and drops off as the effective area of exhaust gas impingement on the turbine blades becomes too small to sufficiently drive the compressor. Note that even though charge flow drops off, EGR fraction continues to increase as the VGT position decreases. The decrease in blade impingement area increases the exhaust pressure and consequently the pressure drop across the EGR valve, driving more exhaust through the EGR loop and increasing EGR fraction.

Charge flow also increases as the EGR valve opening increases at any fixed VGT position, as expected. However, charge flow slightly drops with larger EGR valve openings, since the increase in EGR fraction (or EGR flow) reduces the amount of exhaust gas available to drive the turbine and, consequently, reduces the ability of the compressor to drive fresh air through the system.

The engine used for experimental data is a 6-cylinder 2008 Cummins ISB 6.7l 325 hp diesel engine with a variable-geometry



(a) Inputs to outputs using maps



(b) Inputs to outputs using analytical functions

Fig. 12 Logic flow comparison

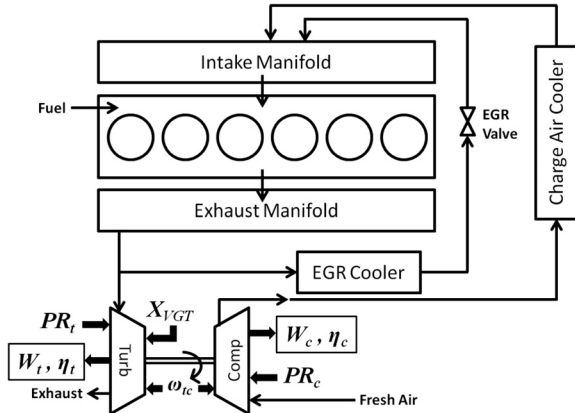


Fig. 13 Experimental engine schematic

Table 7 Engine operating points

Case	Speed (rpm)	Torque (Nm)
1	2300	522
2	1650	407
3	1000	203

turbocharger and cooled exhaust gas recirculation. The turbocharger schematic from Fig. 15(a) is shown in relation to the engine as seen in Fig. 13, again with turbocharger model inputs shown in blue and outputs in red. The engine was run at three operating points, listed in Table 7 and shown on the compressor map in Fig. 15, as well as an engine torque-speed diagram shown in Fig. 16. The MATLAB simulation model was also run at these same three points, both with turbocharger maps and with the analytical

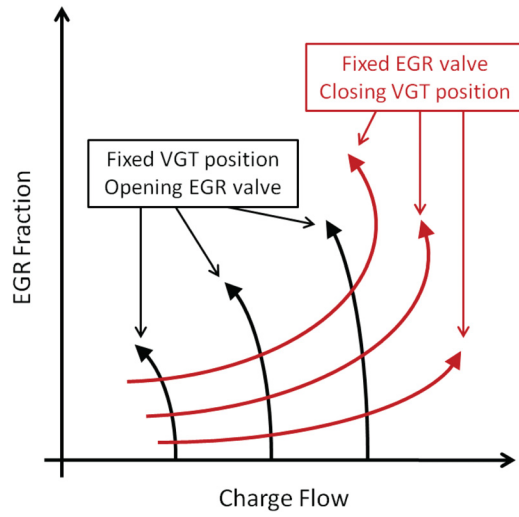


Fig. 14 Example air-handling sweep

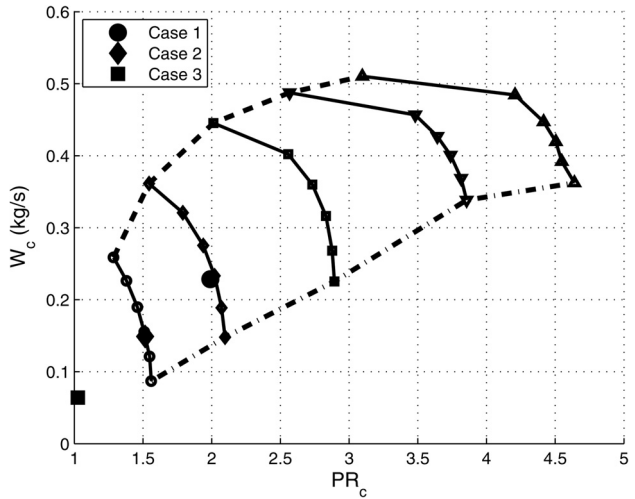


Fig. 15 Operating points on the compressor map

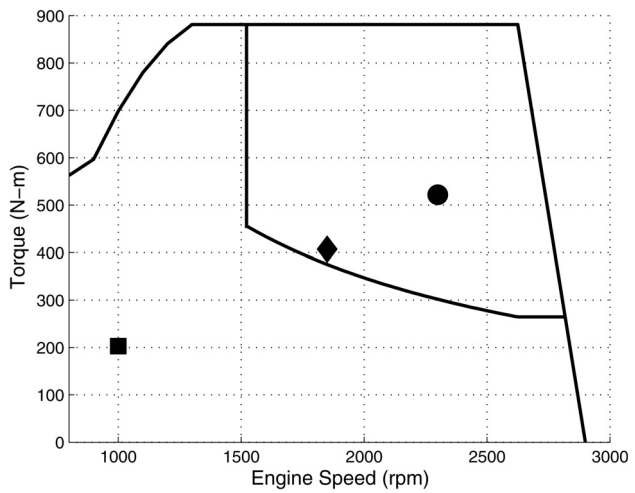
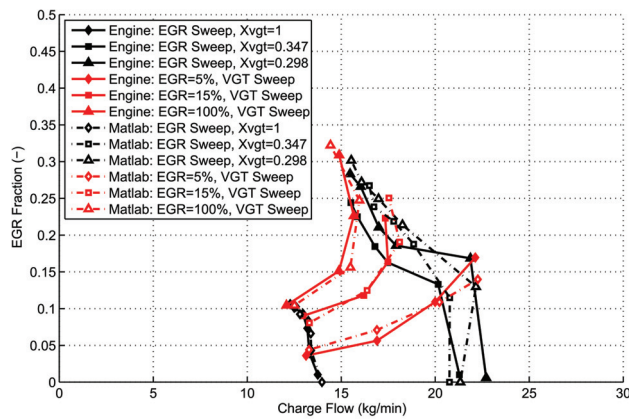
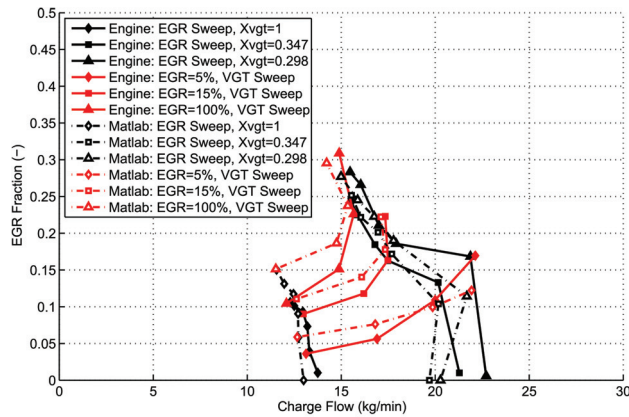


Fig. 16 Operating points on the torque-speed map



(a) Simulation results using maps



(b) Simulation results using functions

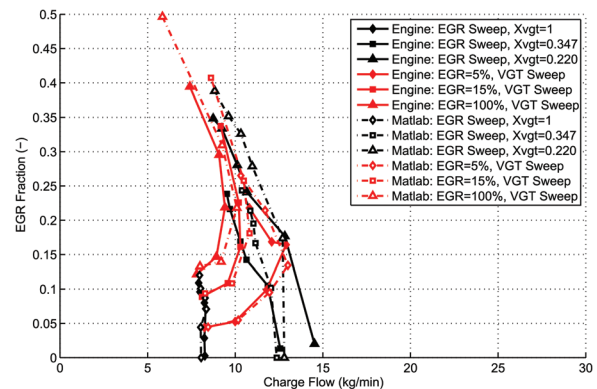
Fig. 17 Case 1 air handling sweep

functions (Eqs. (12), (16), (29), and (33)), using the same EGR valve and VGT nozzle positions that were used during the engine tests.

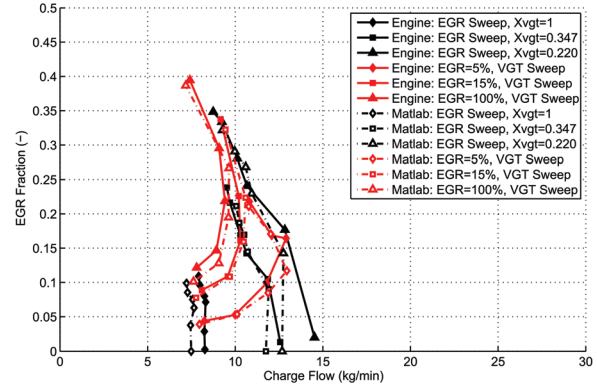
Comparisons of simulation results to experimental engine data are shown in Figs. 17–19. In each set of plots, EGR fraction is plotted against charge flow. Solid lines indicate experimental engine data, and dashed lines indicate simulation data. Figure (a) of each set compares engine data to simulation results when the original turbocharger maps are used and implemented in the MATLAB simulation model as look-up tables, from which mass flows and efficiencies are interpolated based on pressure ratio, speed, and VGT position. Figure (b) of each set is the same air-handling sweep for that operating point, but the MATLAB simulation model uses the simplified analytical turbocharger equations outlined in Secs. 1–4 (Eqs. (13), (17), (29), and (33)), rather than interpolating from the turbocharger maps.

Simulation results for Case 1, shown in Fig. 17, show very good correlation to experimental engine data. As shown in Fig. 17(b), the absolute values from simulation when using simplified functions are very close but do not match the engine data as well as when original map data is used. However, the trends in EGR fraction and charge flow are captured quite well. For Case 2 (Fig. 18(b)), the simulation results using functions also match engine data very well, both in absolute values and in trends.

As we move lower in speed and load to Case 3, it becomes difficult to simulate engine behavior. As shown in Fig. 15, Case 3 lies off the compressor map in a region where both the maps and functions need to be extrapolated. Simulation results for this case are shown in Fig. 19. Note that the scale for charge flow in this case is 3 kg/min to 5 kg/min, rather than 0 to 30 as with Cases 1 and 2. If plotted on the same scale, the air handling sweep would

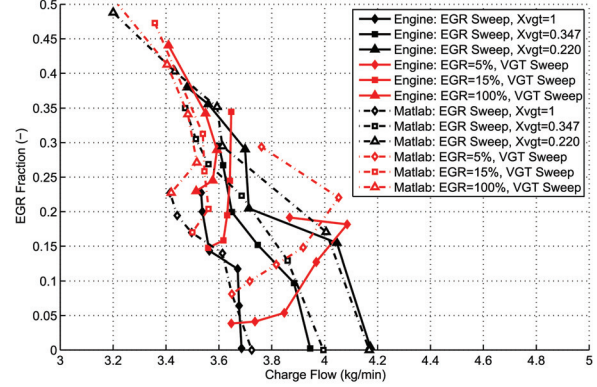


(a) Simulation results using maps

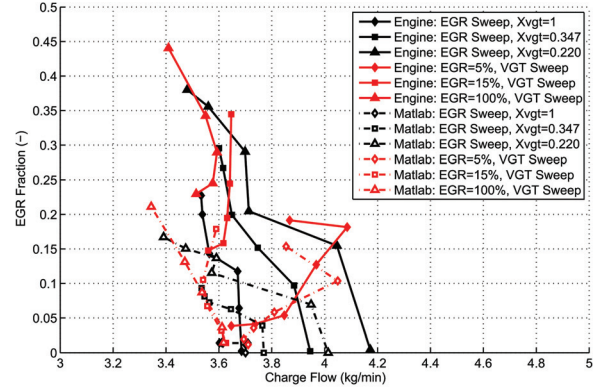


(b) Simulation results using functions

Fig. 18 Case 2 air handling sweep



(a) Simulation results using maps



(b) Simulation results using functions

Fig. 19 Case 3 air handling sweep

Table 8 Case 1 air handling sweep CPU times

X_{vgt}	EGR _{pos} (%)	Using look-up maps	Using functions
1	0	1 min 37 s	31 s
1	5	1 min 27 s	19 s
1	10	1 min 37 s	19 s
1	15	1 min 33 s	18 s
1	30	1 min 30 s	19 s
1	100	1 min 12 s	18 s
0.347	0	3 min 58 s	59 s
0.347	5	55 s	19 s
0.347	10	59 s	15 s
0.347	15	52 s	15 s
0.347	30	53 s	17 s
0.347	100	54 s	19 s
0.298	0	51 s	60 s
0.298	5	52 s	18 s
0.298	10	1 min 7 s	16 s
0.298	15	1 min 4 s	16 s
0.298	30	1 min 9 s	15 s
0.298	100	48 s	19 s
1	5	55 s	19 s
0.511	5	54 s	17 s
0.366	5	1 min 2 s	17 s
0.268	5	53 s	17 s
1	15	1 min 15 s	19 s
0.511	15	1 min 4 s	15 s
0.366	15	49 s	17 s
0.268	15	52 s	16 s
1	100	1 min 10 s	18 s
0.511	100	1 min 19 s	16 s
0.366	100	1 min 3 s	20 s
0.268	100	1 min 3 s	19 s
Average time		1 min 17 s	21 s
Total time		38 min 36 s	10 min 22 s

be almost vertical, indicating almost no authority over charge flow, as small changes in EGR valve or VGT nozzle positions largely impact EGR fraction. Simulation results using turbocharger maps (Fig. 19(a)) and analytical functions (Fig. 19(a)) both struggle to match engine behavior in this region of operation. Though the ranges of EGR fraction seen in operation are not quite matched in simulation, the tail end of each sweep generally follows trends seen in engine data. Case 3 results demonstrate that, as expected, the analytical approach has difficulty at operating locations where the maps also have difficulty, since the analytical functions are determined from non-dimensional representations of the maps themselves.

In addition to being control-amenable, another benefit of using analytical functions to describe turbocharger performance is reduced simulation time. As an example, Case 1 air-handling sweep CPU times are listed in Table 8, each data point in the sweep represented by the combination of actuator settings for the EGR valve and VGT nozzle positions. The simulation times to complete each point as well as the entire air-handling sweep are listed for both map-based calculations and calculations using the analytical functions. Note that both the maps and functions were implemented in the previously mentioned gas exchange model, and several factors contribute to model convergence. The times listed in Table 8 give an indication of the reduction in simulation time possible simply by switching from the turbocharger manufacturer-provided performance maps (i.e., look-up tables) to the analytical functions. For all three cases, simulation time was reduced by at least a factor of 3 when the analytical functions were used.

While the results detailed in this work are for steady-state operation, the implementation of these analytical functions can be extended to transient engine operation as well. Some transient results utilizing the analytical turbocharger functions in a control-oriented gas exchange model are presented in Refs. [39] and [40].

6 Conclusions and Future Work

A turbocharger model consisting of analytical functions was proposed for use in control-oriented modeling. A well-documented non-dimensional approach [33] was used and further developed to accurately describe mass flows and efficiencies of a variable-geometry turbocharger. New contributions include:

- (1) Incorporation of turbocharger shaft speed dependence directly into the non-dimensionalization of the compressor map, simplifying the resulting analytical expressions describing compressor mass flow and efficiency
- (2) Extension of the non-dimensional approach to the turbine

Function fits for both the turbine and compressor correlate well with manufacturer-provided turbocharger data, and results from integrating the simple turbocharger model into a gas exchange model show good agreement with trends in experimental engine data. Future efforts include using this simplified turbocharger model to develop estimation and control strategies for gas exchange processes for multi-cylinder turbocharged diesel engines.

Acknowledgment

This material is based upon work supported by the Department of Energy under Award No. DE-EE0003403. Special thanks to Cummins, Inc., for providing the engine and other experimental equipment, as well as technical support, especially from the following researchers at Cummins Technical Center in Columbus, Indiana: Ray Shute, Tim Frazier, Cheryl Klepser, Don Stanton, Phanindra Garimella, and Rajani Modiyani. The authors also wish to thank the Technical Services staff at the Ray W. Herric Laboratories for their assistance: Fritz Peacock, Bob Brown, Gil Gordon, and Frank Lee.

References

- [1] Heywood, J., 1988, *Internal Combustion Engine Fundamentals*, McGraw-Hill, New York.
- [2] Müller, M., Hendricks, E., and Sorenson, S., 1988, "Mean Value Modelling of Turbocharged Spark Ignition Engines," SAE Paper No. 980784.
- [3] Descombes, G., Pichouron, J., Maroteaux, R., Moreno, N., and Jullien, J., 2002, "Simulation of the Performance of a Variable Geometry Turbocharger for Diesel Engine Road Propulsion," *Int. J. Appl. Thermodyn.*, **5**(3), pp. 139–149.
- [4] Puddu, P., 2010, "Dimensionless Flow Equations for Dynamic Simulation of Turbomachine Components and Fluid Systems," *IMechE J. Power Energy*, **224**(3), pp. 419–431.
- [5] Krasnitski, T., 2006, "Improved Model to Determine Turbine and Compressor Boundary Conditions With the Method of Characteristics," *Int. J. Mech. Sci.*, **48**, pp. 504–516.
- [6] Chauvin, J., Moulin, P., Youssef, B., and Grondin, O., 2008, "Global Airpath Control for a Turbocharged Diesel HCCI Engine," *Oil Gas Sci. Technol.*, **63**(4), pp. 553–561.
- [7] Stefanopoulou, A., Kolmanovsky, I., and Freudenberg, J., 2000, "Control of Variable Geometry Turbocharged Diesel Engines for Reduced Emissions," *IEEE Trans. Control Syst. Technol.*, **8**(4), pp. 733–745.
- [8] Kao, M., and Moskwa, J., 1995, "Turbocharged Diesel Engine Modeling for Nonlinear Engine Control and State Estimation," *ASME J. Dyn. Syst., Meas., Control*, **117**, pp. 20–30.
- [9] Papadimitriou, I., Silvestri, J., Warner, M., and Despujols, B., 2008, "Development of Real-Time Capable Engine Plant Models for Use in HIL Systems," SAE Paper No. 2008-01-0990.
- [10] Kolmanovsky, I., Moraal, P., van Nieuwstadt, M., and Stefanopoulou, A., 1997, "Issues in Modelling and Control of Intake Flow in Variable Geometry Turbocharged Engines," Proceedings of the 18th IFIP conference on system modeling and optimization.
- [11] Jung, M., 2003, "Mean-Value Modelling and Robust Control of the Airpath of a Turbocharged Diesel Engine," Ph.D thesis, University of Cambridge, Cambridge, UK.
- [12] Westin, F., 2005, "Simulation of Turbocharged SI-engines—With Focus on the Turbine," Ph.D thesis, Royal Institute of Technology, Stockholm, Sweden.
- [13] Yang, X., and Zhu, G., 2010, "A Mixed Mean-Value Crank-Based Model of a Dual-Stage Turbocharged SI Engine for Hardware-in-the-Loop Simulation," Proceedings of the 2010 American Control Conference.
- [14] He, Y., 2005, "Development and Validation of a 1D Model of a Turbocharged v6 Diesel Engine Operating Under Steady-State and Transient Conditions," SAE Paper No. 2005-01-3857.
- [15] Zhuge, X. Z. M. Y. W., Zhang, Y., and He, Y., 2009, "Development of an Advanced Turbocharger Simulation Method for Cycle Simulation of Turbocharged Internal Combustion Engines," *IMechE J. Automob. Eng.*, **223**, pp. 661–672.

- [16] Morel, T., and Wahiduzzaman, S., 1996, "Modeling of Diesel Combustion and Emissions," FISITA Proceeding XXVI International Congress, Praha, Czech Republic.
- [17] Kulkarni, A., Shaver, G., Popuri, S., Frazier, T., and Stanton, D., 2009, "Computationally Efficient Whole-Engine Model of a Cummins 2007 Turbocharged Diesel Engine," *ASME J. Eng. Gas Turbines Power*, **132**, p. 022803.
- [18] Modiyani, R., Kocher, L., Van Alstine, D. G., Koeberlein, E., Stricker, K., Meckl, P., and Shaver, G., 2010, "Effect of Intake Valve Closure Modulation on Effective Compression Ratio and Gas Exchange in Modern, Multi-Cylinder Diesel Engines," *Int. J. Engine Res.*, **12**(6), pp. 617–631.
- [19] Serrano, J., Arnau, F., Dolz, V., Tiseira, A., and Cervelló, C., 2008, "A Model of Turbocharger Radial Turbines Appropriate to be Used in Zero- and One-Dimensional Gas Dynamic Codes for Internal Combustion Engines Modelling," *Energy Convers. Manage.*, **49**, pp. 3729–3745.
- [20] Eriksson, L., Nielsen, L., Bergström, J., Bergström, J., Pettersson, F., and Andersson, P., 2002, "Modeling of a Turbocharged SI Engine," *Annu. Rev. Control*, **26**, pp. 129–137.
- [21] Jung, M., Ford, R., Glover, K., Collings, N., Christen, U., and Watts, M., 2002, "Parameterization and Transient Validation of a Variable Geometry Turbocharger for Mean-Value Modeling at Low and Medium Speed-Load Points," SAE Paper No. 2002-01-2729.
- [22] Taitt, D., Garner, C., Swain, E., Bassett, M., Pearson, R., and Turner, J., 2005, "An Automotive Engine Charge-Air Intake Conditioner System: Thermodynamic Analysis of Performance Characteristics," *IMechE J. Automob. Eng.*, **219**, pp. 389–404.
- [23] Joshi, A., James, S., Meckl, P., King, G., and Jennings, K., 2007, "A Comprehensive Physics-Based Model for Medium Duty Diesel Engine With Exhaust Gas Recirculation," Paper No. IMECE2007-42119.
- [24] Jiang, L., Vanier, J., Yilmaz, H., and Stefanopoulou, A., 2009, "Parameterization and Simulation for a Turbocharged Spark Ignition Direct Injection Engine With Variable Valve Timing," SAE Paper No. 2009-01-0680.
- [25] Jankovic, M., Jankovic, M., and Kolmanovsky, I., 2000, "Constructive Lyapunov Control Design for Turbocharged Diesel Engines," *IEEE Trans. Control Syst. Technol.*, **8**(2), pp. 288–299.
- [26] Wang, J., 2008, "Hybrid Robust Air-Path Control for Diesel Engines Operating Conventional and Low Temperature Combustion modes," *IEEE Trans. Control Syst. Technol.*, **16**(6), pp. 1138–1151.
- [27] Das, H., and Dhinagar, S., 2008, "Airpath Modelling and Control for a Turbocharged Diesel Engine," SAE Paper No. 2008-01-0999.
- [28] Yang, M., Zheng, X., Zhang, Y., and Li, Z., 2008, "Improved Performance Prediction Model for Turbocharger Compressor," SAE Paper No. 2008-01-1690.
- [29] Whitfield, A., and Wallace, F., 1975, "Performance Prediction for Automotive Turbocharger Compressors," *Proc. Inst. Mech. Eng.*, **189**(12), pp. 557–565.
- [30] Moraal, P., and Kolmanovsky, I., 1999, "Turbocharger Modeling for Automotive Control Applications," SAE Paper No. 1999-01-0908.
- [31] Filipi, Z., Wang, Y., and Assanis, D., 2001, "Effect of Variable Geometry Turbine (VGT) on Diesel Engine and Vehicle System Transient Response," SAE Paper No. 2001-01-1247.
- [32] Winkler, G., 1977, "Steady-State and Dynamic Modelling of Engine Turbomachinery Systems," Ph.D thesis, University of Bath, Bath, UK.
- [33] Jenson, J., Kristensen, A., Sorenson, S., and Houbak, N., 1991, "Mean Value Modeling of a Small Turbocharged Diesel Engine," SAE Paper No. 910070.
- [34] Sorenson, S., Hendricks, E., Magnusson, S., and Bertelsen, A., 2005, "Compact and Accurate Turbocharger Modelling for Engine Control," SAE Paper No. 2005-01-1942.
- [35] Eriksson, L., 2007, "Modeling and Control of Turbocharged SI and DI Engines," *Oil Gas Sci. Technol.*, **62**(4), pp. 523–538.
- [36] Canova, M., Midlam-Mohler, S., Guezenne, Y., and Rizzoni, G., 2009, "Mean Value Modeling and Analysis of HCCI Diesel Engines With External Mixture Formation," *ASME J. Dyn. Syst., Meas., Control*, **131**, p. 011002.
- [37] Martin, G., Talon, V., Higelin, P., Charlet, A., and Caillol, C., 2009, "Implementing Turbomachinery Physics into Data Map-Based Turbocharger Models," SAE Paper No. 2009-01-0310.
- [38] Martin, G., Talon, V., Peuchant, T., Higelin, P., and Charlet, A., 2009, "Physics Based Diesel Turbocharger Model for Control Purposes," SAE Paper No. 2009-24-0123.
- [39] Kocher, L., Koeberlein, E., Stricker, K., Van Alstine, D. G., and Shaver, G., 2011, "Control-Oriented Modeling of Diesel Engine Gas Exchange," Proceedings of the American Control Conference.
- [40] Kocher, L., Koeberlein, E., Stricker, K., Van Alstine, D. G., and Shaver, G., 2012, "Control-Oriented Gas Exchange Model for Diesel Engines Utilizing Variable Intake Valve Actuation," *ASME J. Dyn. Syst., Meas., Control*, (submitted).